8

Numerical and Experimental Study of Mass Transfer Through Cavitation in Turbomachinery

Rafael Campos-Amezcua[1], Sofiane Khelladi[2],
Zdzislaw Mazur-Czerwiec[1], Farid Bakir[2],
Alfonso Campos-Amezcua[1] and Robert Rey[2]
[1] *Electrical Research Institute, Department of Turbomachinery, Cuernavaca,*
[2]*Arts et Métiers ParisTech, DynFluid Laboratory, Paris,*
[1]*Mexico*
[2]*France*

1. Introduction

The vapour generation in a liquid can be caused by two different mechanisms: following a heat input, thus an increase in temperature at constant pressure, which is well known as the boiling phenomenon, or, at constant temperature, a decrease of pressure, which corresponds to the cavitation phenomenon.
When the liquid pressure decreases below the saturation pressure, some liquid undergoes a phase change, from liquid to vapour. The saturation pressure, p_v, is a fluid property which depends strongly on the fluid temperature. The cavitation phenomenon is manifested, in the fluid flow, by the formation of bubbles, regions of vapour or vapour eddies.
The cavitation phenomenon frequently occurs in hydraulic machines operating under low pressure conditions. The cavitation phenomenon causes several undesirable effects on this type of machines, for example: the noise generated by the mass transfer between the phases, the efficiency loss of the hydraulic machines, and the erosion of certain elements caused by the vapour bubbles collapses near walls. Additionally, it should be mentioned the flow instabilities caused by the vapour appearance, such as alternate blade cavitation and rotating blade cavitation (Campos-Amezcua et al., 2009).
The formation of cavitating structures in the hydraulic machines, their geometry and more generally, their static and dynamic properties, depend on several parameters (Bakir et al., 2003), such as:

- Geometrical conditions: profile, camber, thickness, incidence, and leading edge shape of the blades, as well as the walls roughness.
- Local flow conditions: pressure, velocities, turbulence, the existence of gas micro-bubbles dissolved in the flow.
- Fluid properties: saturation pressure, density, dynamic viscosity and surface tension.

This chapter presents an analysis of the cavitating flows on three axial inducers. These studies include numerical analyses at a range of flow rates and cavitation numbers, which were validated with experimental tests (Campos-Amezcua et al., 2009; Mejri et al., 2006). The obtained results can be summarized of the following way:

1. Experimental results concerning:
   a. Steady state performances: pressure head coefficient and efficiency versus flow rates.
   b. Steady state cavitating behaviour of the studied inducers.
2. Numerical results concerning:
   a. Steady and unsteady states performances: pressure head coefficient and efficiency versus flow rates.
   b. Steady and unsteady states cavitating behaviour of the studied inducers.
   c. Vapour distributions and other numerical results, which enable to explain the cavitating behaviour for these inducers.
   d. The fluid flow instabilities generated by the presence of vapour.

The numerical simulations were performed using the commercial code *Fluent*, which is based on a cell-centred finite-volume method. The cavitation model used for the calculations assumes a thermal equilibrium between the phases. It is based on the classical conservation equations of the vapour phase and a mixture phase, with mass transfer due to the cavitation, which appears as a source term and a sink term in the vapour mass fraction equation. The mass transfer rate is derived from a simplified Rayleigh–Plesset model for bubble dynamics.
The experimental tests were carried out at the DynFluid Laboratory of Arts et Métiers ParisTech.
Next, the different cases studied in this work, to understand the cavitating behaviour of the inducers, are described:

a. Cavitating flow through venturi geometry.
   This part presents the numerical validation of the cavitating flow through a 2D simple geometry. On the one hand, the numerical results demonstrate the influence of the turbulence model to predict instabilities in non-homogeneous flows. On the other hand, the intrinsic instabilities were detected and compared to experimental data.
b. Analysis of cavitating flow in two-dimensional inducers – blades cascades.
   This part presents the steady and unsteady numerical study carried out on two blades cascades: first, on a two-blade aircraft inducer, and then, on a three-blade industrial inducer, see Fig. 1. This analysis confirms the influence of blades number and the solidity on the behaviour of the instabilities of cavitating flow. Various forms and behaviours of vapour have been observed in the blades cascades, such as: stable blade cavitation, alternate blade cavitation and rotating blade cavitation.
c. Experimental study and numerical analysis of the cavitating flow in three-dimensional inducers.
   This part presents the steady and unsteady numerical simulations, and experimental investigations in steady state of the cavitating flow through of the three inducers presented in the Fig. 1. The flow behaviour in the inducers is modified by the appearance of the cavitation on the leading edge. These cavitating behaviours change with respect to the operating conditions of the inducer: flow rates and cavitation levels.

Fig. 1 shows the three inducers used for the numerical and experimental study in cavitating regime, and the Table 1 presents the main characteristics of these inducers.

2. Numerical method

The commercial code used for all simulations was *Fluent*. This code employs a cell–centred finite–volume method that allows the use of computational elements with arbitrary

(a) (b) (c)

Fig. 1. Inducers used for the numerical and experimental study in cavitating regime.
(a) Three-blade industrial inducer with β=16° (b) Three-blade industrial inducer with β=8°
(c) Two-blade aircraft inducer with β=4°

Parameters	**Industrial inducer** ***β=16°***	**Industrial inducer** ***β=8°***	**Aircraft inducer** ***β=4°***
Maximal efficiency	57%	54.1%	15.5%
Nominal flow rate coeff.	0.159	0.076	0.014
Nominal head coeff.	0.310	0.228	0.188
Blade number	3	3	2
Blade tip angle	16°	8°	4°
Tip solidity	2.95	2.45	3
Rotational velocity	1,450 RPM	1,450 RPM	8,000 RPM

Table 1. Principal characteristics of inducers used for the cavitating analyses

Nomenclature

D	diameter
f_{cav}	detachment frequency
l	blade chord length
l_{cav}	cavitation length
p	pressure
P_v	saturation pressure
Q	flow rate
R	radius
St	Strouhal number
T	cycle period
t	time
U	tangential velocity
v	velocity magnitude

Greek

a	vapour volume fraction
β	blade tip angle
η	efficiency
γ	vapour mass fraction
Φ	flow coefficient
Ψ	head coefficient
ω	rotational speed
ρ	density
σ	cavitation number
σ_s	surface tension

Subscript

1, 2	inlet, outlet
a	axial direction
B	bubble
c	condensation
cav	cavitation
e	vaporization
g	gas
l	liquid
nom	nominal
t	blade tip
v	vapour

polyhedral shape. Convective terms were discretized using the second–order upwind scheme. The velocity–pressure coupling and overall solution procedure were based on a SIMPLE type segregated algorithm adapted to unstructured grids. The discretized equations were solved using point-wise Gauss–Seidel iterations, and an algebraic multi–grid method accelerates the solution convergence. A more detailed description of the numerical method is available in Kim et al. (1998).
The convergence criteria in the present numerical analysis were at least of three orders of magnitude, for the mass conservation imbalance and momentum equation residuals, which are deemed sufficient for most steady flow solutions. On the other hand, the residual values were defined at least of six orders of magnitude, for the unsteady flow solutions.

2.1 Cavitation model

The cavitation model used for this study was developed by Singhal et al. (2002). It takes into account all first–order effects (i.e., the phase change, the bubble dynamics, the turbulent pressure fluctuations, and the non–condensable gases). The influence of slip velocity between the liquid and the vapour phases was not considering.
For the multi–phase flow solution, the single–fluid mixture model was employed. The mixture model solves the continuity and momentum equations for the mixture, and the volume fraction equation for the secondary phases. The cavitation model consists of solving the standard incompressible Reynolds–Average Navier–Stokes equations (RANS) using a conventional turbulence model (e.g., κ–ε turbulence model).
The working fluid is assumed to be a mixture of liquid, vapour and non-condensable gas (NCG). The mixture density is a function of vapour and NCG mass fractions, γ_v and γ_g, which is computed by solving a transport equation, coupled with the mass and momentum conservation equations. The mixture density is defined by:

$$\frac{1}{\rho} = \frac{\gamma_v}{\rho_v} + \frac{\gamma_g}{\rho_g} + \frac{1-\gamma_v-\gamma_g}{\rho_l} \tag{1}$$

With

$$\gamma_v = \frac{\alpha_v \rho_v}{\rho}, \quad \gamma_g = \frac{\alpha_g \rho_g}{\rho}, \quad and \quad \gamma_l = \frac{\alpha_l \rho_l}{\rho} = 1-\gamma_v-\gamma_g \tag{2}$$

where a_g, a_l and a_v are the non–condensable gas, liquid and local vapour volume fraction, respectively; and $a = a_g + a_v$ is the global vapour volume fraction.
The vapour mass fraction is governed by the transport equation given by:

$$\frac{\partial}{\partial t}(\rho\gamma) + \nabla \cdot (\rho \boldsymbol{v}\gamma) = \nabla \cdot (\Gamma \nabla \gamma) + R_e - R_c \tag{3}$$

where $\boldsymbol{v}$ is the velocity vector of the vapour phase; Γ is the effective exchange coefficient, and R_e and R_c are the vapour generation and condensation rate terms. The above formulation employs a homogenous flow approach.
In a flowing liquid, with null slip velocity between the phases, the bubble dynamics equation can be derived from the generalized Rayleigh–Plesset equation as:

$$R_B \frac{D^2 R_B}{Dt^2} + \frac{2}{3}\left(\frac{DR_B}{Dt}\right)^2 = \frac{P_B - P}{\rho_l} - \frac{4\nu_l}{R_B}\dot{R_B} - \frac{2\sigma_s}{\rho_l R_B} \tag{4}$$

This equation provides a physical approach to introduce the effects of bubble dynamics into the cavitation model. In fact, it can be considered to be an equation for vapour propagation and, hence, mixture density.

Using the Rayleigh–Plesset equation without the viscous damping and surface tension terms and coupling with the two-phase continuity equations (liquid phase, vapour phase and mixture), the expression for the net phase change rate, R, is finally obtained as:

$$R = (n4\pi)^{1/3}\frac{\rho_v\rho_l}{\rho}\left[\frac{2}{3}\left(\frac{P_B - P}{\rho_l}\right) - \frac{2}{3}R_B\frac{D^2R_B}{Dt^2}\right]^{1/2} \tag{5}$$

Using this equation and ignoring the second–order derivative of R_B, the simplified equation for vapour transport is obtained as:

$$\frac{\partial}{\partial t}(\rho\gamma) + \nabla\cdot(\rho\gamma\vec{v}) = (n4\pi)^{1/3}(3\alpha)^{2/3}\frac{\rho_v\rho_l}{\rho}\left[\frac{2}{3}\left(\frac{P_B - P}{\rho_l}\right)\right]^{1/2} \tag{6}$$

The global vapour volume fraction, a, can be related to the bubble number density, n, and radius of bubble R_B as:

$$\alpha_v = n\cdot(4/3)\cdot\pi\cdot R_B^3 \tag{7}$$

Turbulent effects are considered using a simply raising of the phase change threshold pressure value as:

$$P_v = P_{sat} + 0.195\cdot\rho\cdot\kappa \tag{8}$$

Finally, with the consideration of the NCG effect, and the turbulent effects, the phase change rate expressions are derived from the reduced form of Rayleigh–Plesset equation of bubble dynamics as:

$$R_e = C_e\frac{\sqrt{\kappa}}{\sigma_s}\rho_v\rho_l\left[\frac{2}{3}\frac{P_v - P}{\rho_l}\right]^{1/2}\left(1 - \gamma_v - \gamma_g\right) \tag{9}$$

$$R_c = C_c\frac{\sqrt{\kappa}}{\sigma_s}\rho_l\rho_l\left[\frac{2}{3}\frac{P - P_v}{\rho}\right]^{1/2}\gamma_v \tag{10}$$

where: C_e=*0.02* and C_c=*0.01* are empirical coefficients and κ is the local turbulent kinetic energy. A more detailed description of the cavitation model is available in Singhal et al. (2002).

2.2 RNG κ–ε model

This model was developed by Yakhot & Orszag (1986). It uses the Re–Normalisation Group (RNG) methods to renormalize the Navier–Stokes equations, and take into account the effects of smaller scales of motion. The RNG κ–ε model is derived from the standard κ–ε model. The main difference is the form of the dissipation of the kinetic turbulent energy equation.

The turbulence kinetic energy, κ, and its rate of dissipation, ε, are obtained from the following transport equations:

$$\frac{\partial}{\partial t}(\rho\kappa) + \frac{\partial}{\partial x_i}(\rho\kappa u_i) = \frac{\partial}{\partial x_j}\left[\left(\mu + \frac{\mu_t}{\sigma_\kappa}\right)\frac{\partial \kappa}{\partial x_j}\right] + P_\kappa - \rho\varepsilon \tag{11}$$

$$\frac{\partial}{\partial t}(\rho\varepsilon) + \frac{\partial}{\partial x_i}(\rho\varepsilon u_i) = \frac{\partial}{\partial x_j}\left[\left(\mu + \frac{\mu_t}{\sigma_\varepsilon}\right)\frac{\partial \varepsilon}{\partial x_j}\right] + C_{1\varepsilon}^{*}\frac{\varepsilon}{\kappa}P_\kappa - C_{2\varepsilon}\rho\frac{\varepsilon^2}{\kappa} \tag{12}$$

where

$$C_{1\varepsilon}^{*} = C_{1\varepsilon} - \frac{C_\kappa \eta^3(1-\eta/\eta_0)}{1+\beta\eta^3}, \quad \eta = \frac{S\kappa}{\varepsilon}, \quad \text{and} \quad S = \left(2S_{ij}S_{ij}\right)^{1/2}$$

P_κ represents the production of turbulence kinetic energy and is defined as:

$$P_\kappa = -\rho\overline{u_i' u_j'}\frac{\partial u_j}{\partial u_i} \tag{13}$$

The turbulent viscosity, μ_t, is given by:

$$\mu_t = \rho C_\mu \frac{\kappa^2}{\varepsilon} \tag{14}$$

The constants of the model are: $C_\mu = 0.0845$, $C_{1\varepsilon} = 1.42$, $C_{2\varepsilon} = 1.68$, $\sigma_\mu = \sigma_\varepsilon = 0.7194$, $\eta_0 = 4.38$, $\beta = 0.012$.

2.3 RNG κ–ε modified model

This turbulent model is an adaptation from the RNG κ–ε model. The modification concerns the reduction, in the high vapour volume fraction regions, of the effective viscosity, $\mu_{eff}=\mu_{flow}+\mu_t$. For this purpose, the mixture turbulent viscosity is given by:

$$\mu_t = f(\rho)C_\mu \frac{\kappa^2}{\varepsilon} \tag{15}$$

where mixture density function, $f(\rho)$, is given by:

$$f(\rho) = \rho_v + \left(\frac{\rho_v - \rho}{\rho_v - \rho_l}\right)^n (\rho_l - \rho_v) \quad where \quad n > 1 \tag{16}$$

This model was proposed by Reboud et al. (1998). This one allows the formation of the re-entrant jet which causes the vapour fluctuations of the cavitating flow in a venturi. The RNG κ–ε modified model has been implemented using a User's Defined Function supplied by *Fluent*.

3. Cases of study

To understand the cavitation phenomenon and calibrate the numerical code used for the analysis of the cavitating flows; first, the numerical analysis was performed on a simplified geometry. The numerical results were compared with experimental data available in references.

After that, the analysis was extended to cavitating flows in two blades cascades with different blades number and solidities. The main purpose of this study was to detect the instabilities of cavitating flow, such as: alternate blade cavitation and rotating blade cavitation.

Finally, the experimental and numerical analyses of cavitating flow were realized in three dimensions. The numerical simulations were developed in steady and unsteady states, and experimental investigations were realized only in steady state.

All the numerical simulations have used water at 300 *K* as the working fluid. The liquid density and the vapour density are ρ_l=1,000 kg/m^3 and ρ_v=0.5542 kg/m^3, respectively. The liquid viscosity and the vapour viscosity are μ_l=1E-3 $Pa{\cdot}s$ and μ_l=1.34E-5 $Pa{\cdot}s$, respectively. The saturation pressure is p_v=2,340 *Pa* and surface tension is σ_s=0.0717 *N/m*. Finally, the non-condensable gas was defined as γ_g= 15 *ppm*.

3.1 Numerical analysis of the cavitating flow through venturi type duct

This section presents the calibration of numerical code and the validation of obtained results for a cavitating flow in a venturi duct with convergence and divergence angles of 18° and 8°, respectively, see Fig. 2(a). The experimental study on this geometry was conducted by (Stutz & Reboud, 2000), who used double optical probes to measure the vapour fraction and the velocity. They have observed that the cavitating flow has an unsteady behaviour with cyclic fluctuations caused by the detachment of the cavitation.

Fig. 2(b) shows the computational grid, which is a structured mesh of 400 X 100 cells. A special refinement was used near the venturi throat and the lower wall, where it is assumed that cavitation will occur.

All simulations were carried out for a constant flow rate, the inlet velocity was fixed to u_1=*7.9 m/s*. The pressure outlet, p_2, was varied to have different cavitation conditions.

Two turbulence models were tested: first, the RNG κ–ε model, and then, the RNG κ–ε modified model. In both cases, the near-wall regions were treated by the wall function method.

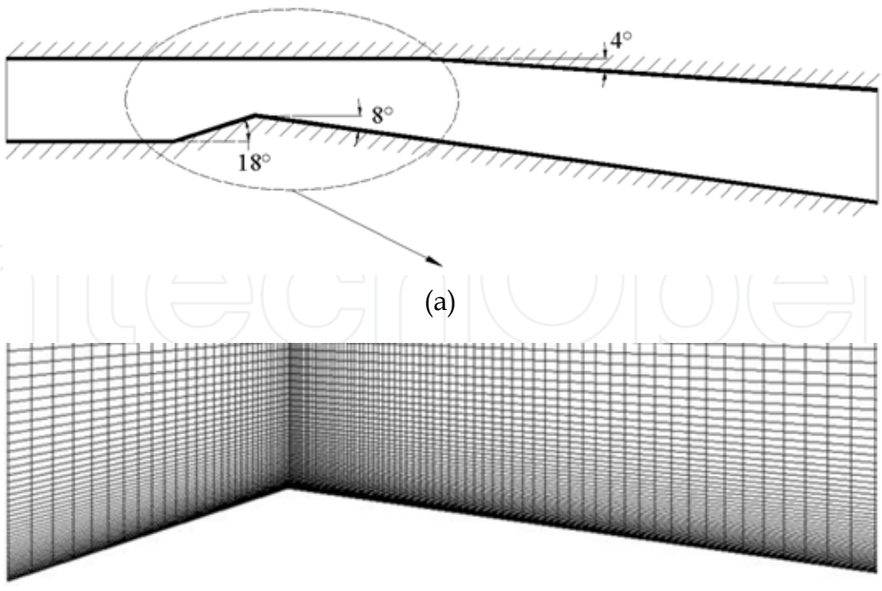

(a)

(b)

Fig. 2. Venturi type duct: (a) Computational domain, and (b) Grid distribution near venturi throat

3.1.1 Numerical results

The cavitating flow in the venturi type duct was characterized using the pressure coefficient, C_p, the cavitation number, σ, and the Strouhal number, St, defined as:

$$C_p = \frac{p - p_{ref}}{1/2 \cdot \rho_l \cdot v_1^2}, \quad \sigma = \frac{p_1 - p_v}{1/2 \cdot \rho_l \cdot v_1^2} \quad and \quad St = \frac{f_{cav} \cdot \overline{l_{cav}}}{v_1} \tag{17}$$

where $\overline{l_{cav}}$ is the time average of l_{cav}.

Preliminary 2D computations suggest a strong interaction of the turbulence and the unsteady cavitation at the venturi throat.

3.1.1.1 RNG κ–ε turbulence model

The first unsteady simulations were carried out using the classical RNG κ –ε model. These numerical results did not reproduce the well-known instabilities of this configuration. The results show, after an unsteady numerical behaviour, a steady cavitation with l_{cav} constant for all the times. This cavity remains attached on the lower wall downstream of the venturi throat. This vapour region grows when σ is reduced, but it remains stable.

The cavitation detachment could not be modelled appropriately. The reason is that RNG κ –ε model overestimates the turbulent viscosity in the cavitation region. Hence, the re-entrant jet is stopped at cavitation sheet closure and then, it could not incite the cavitation break off.

The RNG κ –ε model was originally conceived to fully incompressible fluids, and no particular correction was applied in the case of the highly compressible two-phase mixture. Therefore, the fluid compressibility is only taken into account in the turbulence equations through the mixture density changes (Wilcox, 1998).

3.1.1.2 RNG κ–ε modified turbulence model

On the other hand, other calculations were performed using the RNG κ –ε modified model. The results show an unstable flow due to the vapour detachment, as it was observed experimentally. The modification of turbulent viscosity allows the detachment of the cavitation caused by a re-entrant jet, which appears on the lower divergent wall. The re-entrant jet goes from cavitation sheet closure toward the venturi throat in the opposite direction to the main flow, which lets the detachment of the cavitation from the wall, see Fig. 3. Thus, the cavitation can be convected in the main flow, where it will be collapsed downstream.

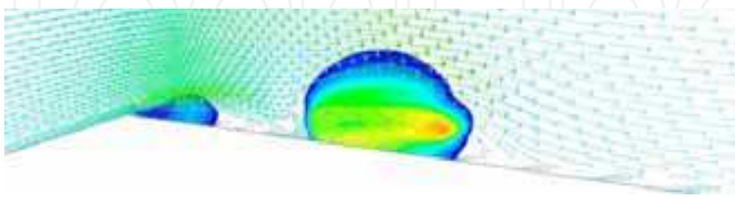

Fig. 3. Contours of vapour fraction ($\alpha \geq 10\%$) and velocity vectors near to venturi throat at $t=0.273 \cdot t_{ref}$ and $\sigma=2.45$. Calculations using RNG κ –ε modified model

The cavitation detachment cycles can be observed, for σ values of 2.45, 2.34, and 2.30, in Fig. 4. This figure shows that the cavitation length, l_{cav}, increases while the cavitation number, σ, and the detachment frequency, f_{cav}, decrease. Generally, the cavitation detachment cycle is composed of the following steps, see the cycle of σ=2.45 in Fig. 4:

Fig. 4. Contours of vapour volume fraction (a≥10%). Vapour detachment cycle calculated for three cavitation numbers. Calculations using RNG κ–ε modified model, t_{ref}=65.8E-3 *s*

1. A very small vapour region appears at the venturi throat (from t=0.023·t_{ref} to t=0.046·t_{ref}).
2. The attached vapour region grows at the downstream venturi throat (from t=0.068·t_{ref} to t=0.137·t_{ref}).
3. A jet flow is generated along the lower wall in the vapour region and goes from cavitation closure towards the venturi throat. The interaction between this re-entrant jet and the interface liquid-vapour causes the detachment of the cavitation (from t=0.160·t_{ref} to t=0.228·t_{ref}).
4. The generated vapour region is convected in the main flow (from t=0.251·t_{ref} to t=0.273·t_{ref}) and (from t=0.023·t_{ref} to t=0.068·t_{ref}).
5. The cavitation collapses downstream (from t=0.091·t_{ref} to t=0.114·t_{ref}).

Fig. 5(a) shows the spectral analysis of the upstream static pressure behaviour *(*σ*=2.45*) which is disturbed by the cavitation detachment. The cavitating flow has a cyclic behaviour with a frequency of cavitation detachment of about f_{cav}*=60 Hz*. The numerical results were compared with the experimental data obtained for the same geometry. Although the vapour volume fraction obtained numerically is higher than the reference data, there is a good agreement if the vapour detachment frequencies are compared, see Fig. 4(b).

Table 2 summarizes the main characteristics of the vapour detachment cycles. According to the experimental data, the detachment frequencies are inversely proportional to the cavitation lengths, and so the Strouhal number remains constant for all the cavitation numbers, St=0.27. The cavitation length was measured at twelve instants of the cavitating period and so, the average value was obtained.

3.2 Numerical analysis of the unsteady cavitating flow in two blades cascades

This part presents the numerical study carried out on two blades cascades: first, on a two-blade aircraft inducer with a blade tip angle of 4°, and then, on a three-blade industrial inducer with a blade tip angle of 8°, see Fig. 1.

3.2.1 Geometrical model and grid generation

The numerical domain, for both cases, has been divided into three sub-domains in order to impose moving mesh conditions. Fig. 6(a) shows the three computational sub-domains of whole numerical model, defined as: upstream region (A), inter-blades region (B), and downstream region (C). Tangential velocity was imposed in the moving region (B) using a sliding mesh technique, whereas (A) and (C) regions were defined as static.

Boundary conditions at the domain inlet and outlet were imposed far enough (15·l), from the leading and trailing edges, respectively, in order to avoid influencing the final results. The used boundary conditions are the following:

a. Constant velocity at the inlet. The nominal flow corresponds to a null incidence angle.
b. Constant static pressure at the outlet. This value has been modified for to get diverse cavitation conditions.
c. Non-slip conditions at the blades boundaries.
d. Sliding conditions at the interfaces (A)–(B) and (B)–(C).
e. Cyclic conditions were applied at two or three successive blades, depending of the analyzed inducer.

By way of example, the Fig. 6(b) shows the computational grid of two-blade inducer. The mesh was generated with a rectangle–like structured grid. An independence grid study was

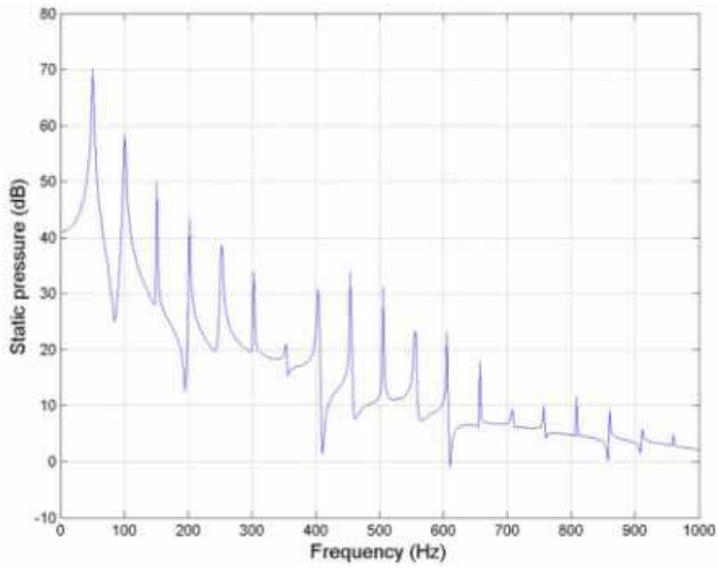

(a)

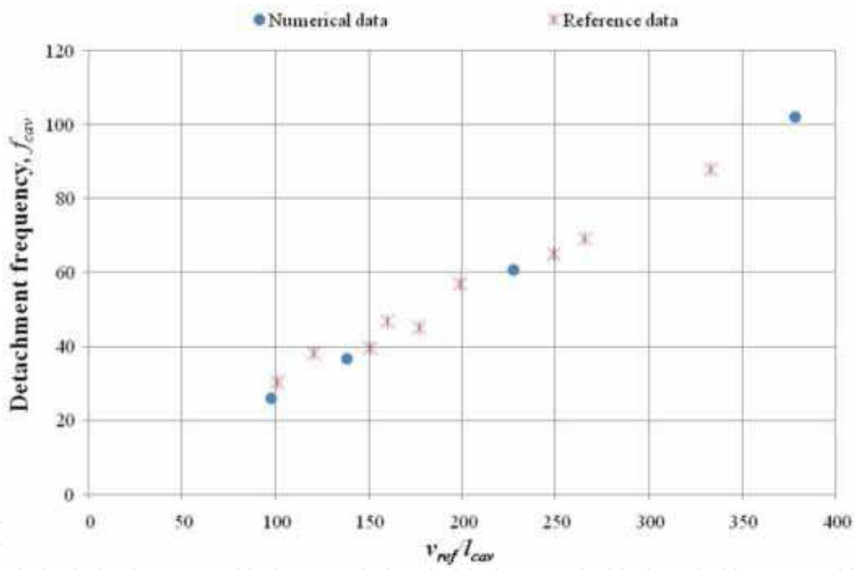

(b)

Fig. 5. (a) Spectral analysis of the upstream static pressure (σ=2.45). (b) Comparison of numerical results and experimental data (Stutz & Reboud, 2000)

σ	T_{cav} (s)	f_{cav} (Hz)	l_{cav}	St
2.61	9.8e-3	102.0	20.90	0.27
2.45	16.5e-3	60.6	34.77	0.27
2.34	27.3e-3	36.6	57.20	0.27
2.30	38.6e-3	25.9	81.02	0.27

Table 2. Characteristics of the cycles of vapour detachment

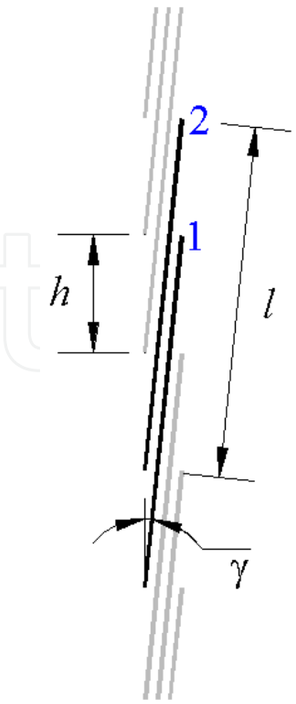

(a) Two-blade cascade

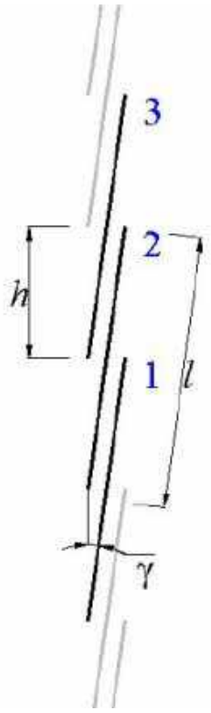

(b) Three-blade cascade

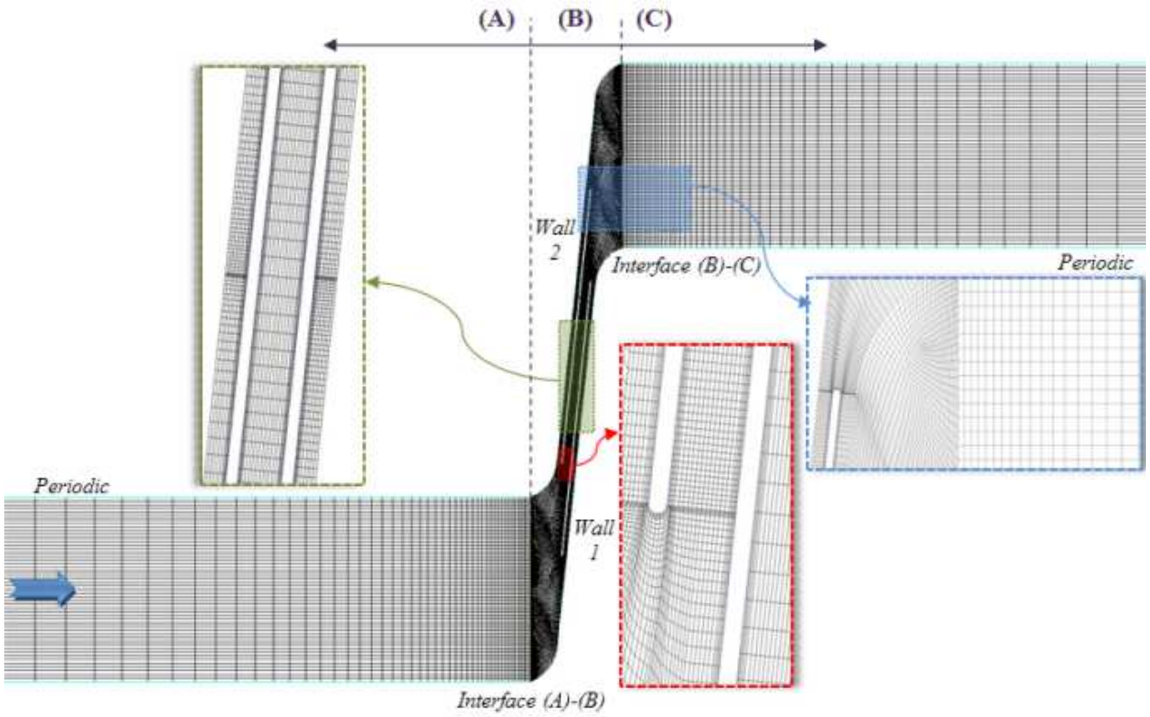

(c) Boundary condition and near-wall mesh resolution

Fig. 6. Blades cascades corresponding to the inducers studied, see Fig. 1

carried out on non-cavitating flow. Three meshes were tested: a coarse mesh (300X50), a fine mesh (500X50), and a refined mesh (650X50). The first coarse mesh presented the backflow at outlet domain because of very important aspect ratio upstream and downstream regions. The fine and refined meshes presented similar results, but the fine mesh reaches the solution faster than the refined mesh; for this reason, the fine mesh was selected for realize all calculations. Boundary layer meshing was used to ensure sufficient refinement near the walls and thus a small dimensionless factor y^+. First cell distance was imposed to 1 *mm*, with a growth rate of 1.2 which allowed values of y^+ between 6 and 51.

3.2.2 Numerical results

The unsteady cavitating flow was characterized by the cavitation number, σ, and the Strouhal number, *St*, defined in (17); and by the head coefficient, Ψ, and the flow coefficient, Φ, given by:

$$\Psi = \frac{P_2 - P_1}{1/2 \cdot \rho_l \cdot v_1^2} \quad and \quad \Phi = \frac{(C_a)_1}{C_t} \tag{18}$$

3.2.2.1 Stable blade cavitation

Calculations of unsteady cavitating flow were carried out for four flow rates over the blades cascade of a two–blade inducer and for three flow rates over the blades cascade of a three–blade inducer, see Fig. 7. En general, the results present two small regions of vapour, at high values of σ, on the leading edge of suction side. The regions of vapour are symmetric, for all the time and all the values of σ. The vapour region increases as σ decreases, until these regions of vapour become large enough to block the flow channel, resulting in the performance drop of inducer, see Fig. 7.

Fig. 8 presents, for Φ=*0.056*, the regions of vapour corresponding to diverse values of σ. This figure shows that the cavitation begins with very small regions of vapour which appear on the leading edge of the blade, on the suction side. The regions of vapour have a steady behaviour, for values of σ between σ=*0.723* and σ=*0.219*. This stable behaviour is characterized by a symmetrical cavitation attached to each blade. The cavitation length grows gradually as σ decreases. When σ decreases even more, the regions of vapour increase and it obstruct the flow channel. So, at σ=*0.219*, the cavitation length containing α≥*10%* of vapour takes, approximately, *50%* of the blade spacing, *h*. Consequently, the alternate blade cavitation appears when the cavitation number decreases to σ=*0.174* and this asymmetrical cavitation continue to σ=*0.140*. After that, for σ=*0.114*, the cavitation becomes symmetrical on both blades and large enough to produce the performances drop of inducer.

Alternate blade cavitation is a phenomenon in which the cavitation length on the blades changes alternately from blade to blade. According to (Tsujimoto, 2005) the alternate blade cavitation starts to develop when the cavitation length exceeds about *65%* of the blade spacing: $(l_{cav}/h) \geq 65\%$. So, the incidence angle to the neighbouring blade decreases and, hence the cavitation length on the neighbouring blade decreases also. Then the incidence angle of the original blade increases and the cavitation length on it also increases.

The cavitation behaviour for Φ=*0.042* presents the same patron of cavitation than for Φ=*0.*056; after a symmetrical blade cavitation, the alternate blade cavitation starts as soon as the l_{cav}/h ratio is higher than 65%, i.e. to σ=*0.156*.

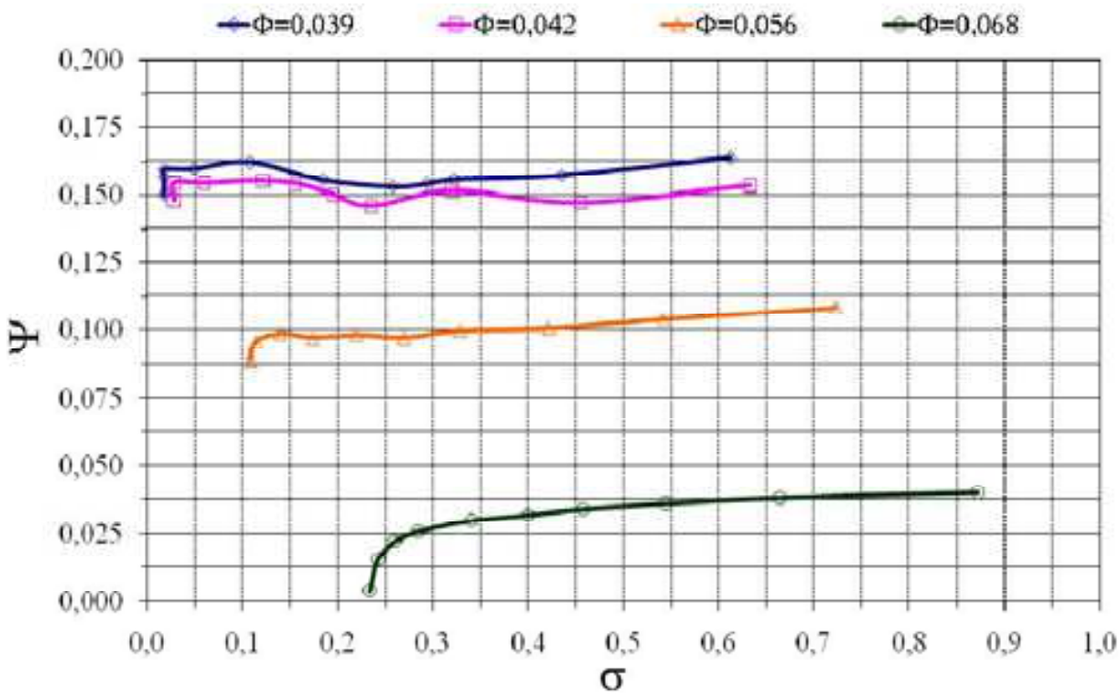

(a) Two-blade inducer

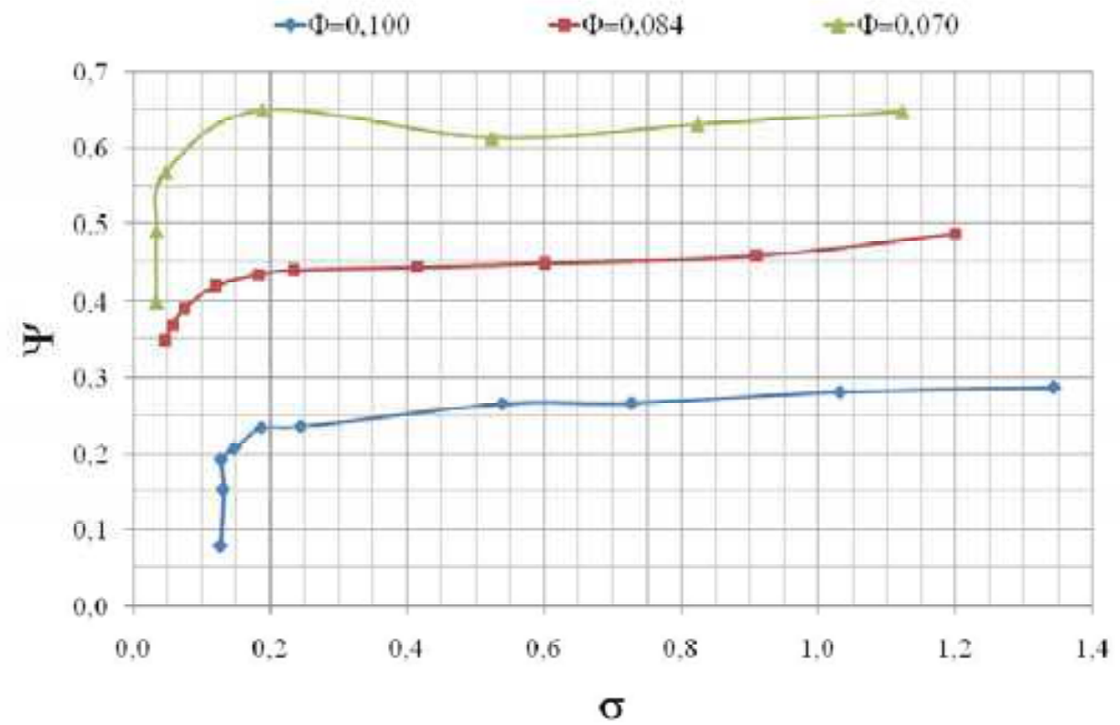

(b) Three-blade inducer

Fig. 7. Curves of the performance drop inducer

However, the alternate blade cavitation was not detected in the three-blade inducer, this agrees with experimental observations which have noted this instability only on inducers with pair blades number.

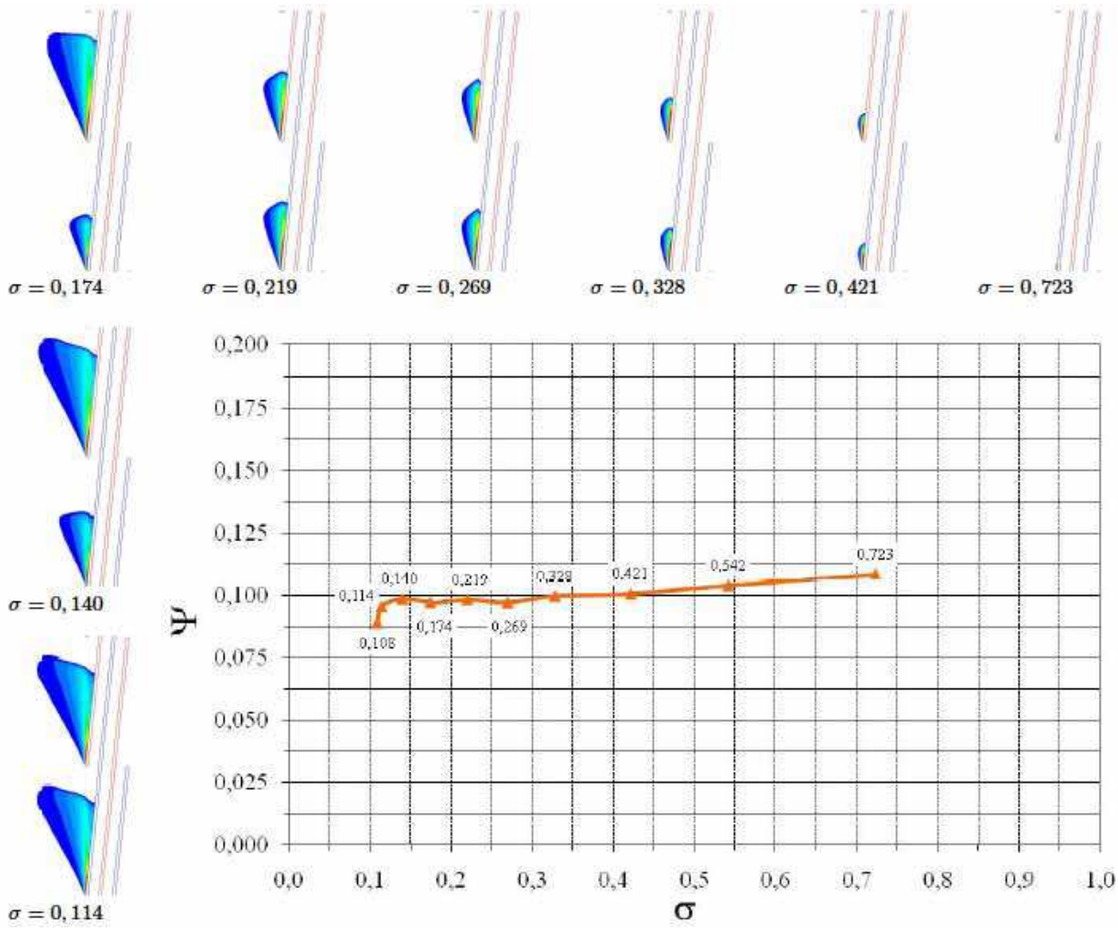

Fig. 8. Curve of the performance drop (Φ=*0.056*) and pictures of the regions of vapour (a≥*10%*) corresponding to diverse values of σ. Calculations using RNG κ–ε model

3.2.2.2 Unstable blade cavitation

The numerical results show the appearance of the rotating blade cavitation to a low flow rate (Φ=*0.039*). As it was observed for the flow rates analysed previously, the cavitation has diverse forms which vary as σ; e.g., for Φ=*0.039*, symmetrical cavitations were observed for high values of the cavitation number (σ≥*0.294*). However, as soon as the cavitation number was decreased to σ=*0.258*, the rotating blade cavitation was occurred. After that, the cavitation became symmetrical on both blades, for cavitation numbers lower than σ<*0.185*.
Fig. 9 shows the contours of vapour fraction (a=*10%* and σ=*0.258*) at different times, with the purpose of observing a cycle of the rotating blade cavitation, T_{cav}. In monitoring the evolution of the cavitation on blade **1**, it is observed that the cavitation length is the same on both blades at t=*0.5*·T_{cav} and t=*1.0*·T_{cav}. In the beginning of the cycle, the cavitation length on the blade **1**, $l_{cav\text{-}b1}$, decreases with the time. So, at t=*0.267*·T_{cav}, the size of $l_{cav\text{-}b1}$ is the smallest on the blade **1**, while the size of $l_{cav\text{-}b2}$ becomes the largest on the blade **2**. The cavitation

length on the blade **2** is inversed to the one on the blade **1**. So, $l_{cav\text{-}b2}$ decreases from $t=0.267 \cdot T_{cav}$ to $t=0.777 \cdot T_{cav}$, where $l_{cav\text{-}b2}$ is the smallest on the blade **2** and $l_{cav\text{-}b1}$ is the largest on blade **1**.

Blade cascade	Φ	σ	f_{cav}	f_{cav}/f_{ω}	T_{cav}
Two-blade	0.039	0.258	9.1 *Hz*	0.068	0.110 *s*
Three-blade	0.070	0.189	1 *Hz*	0.041	1.000 *s*
	0.084	0.184	1.59 *Hz*	0.066	0.630 *s*

Table 3. Comparison of frequencies of vapour detachment in the studied blades cascades

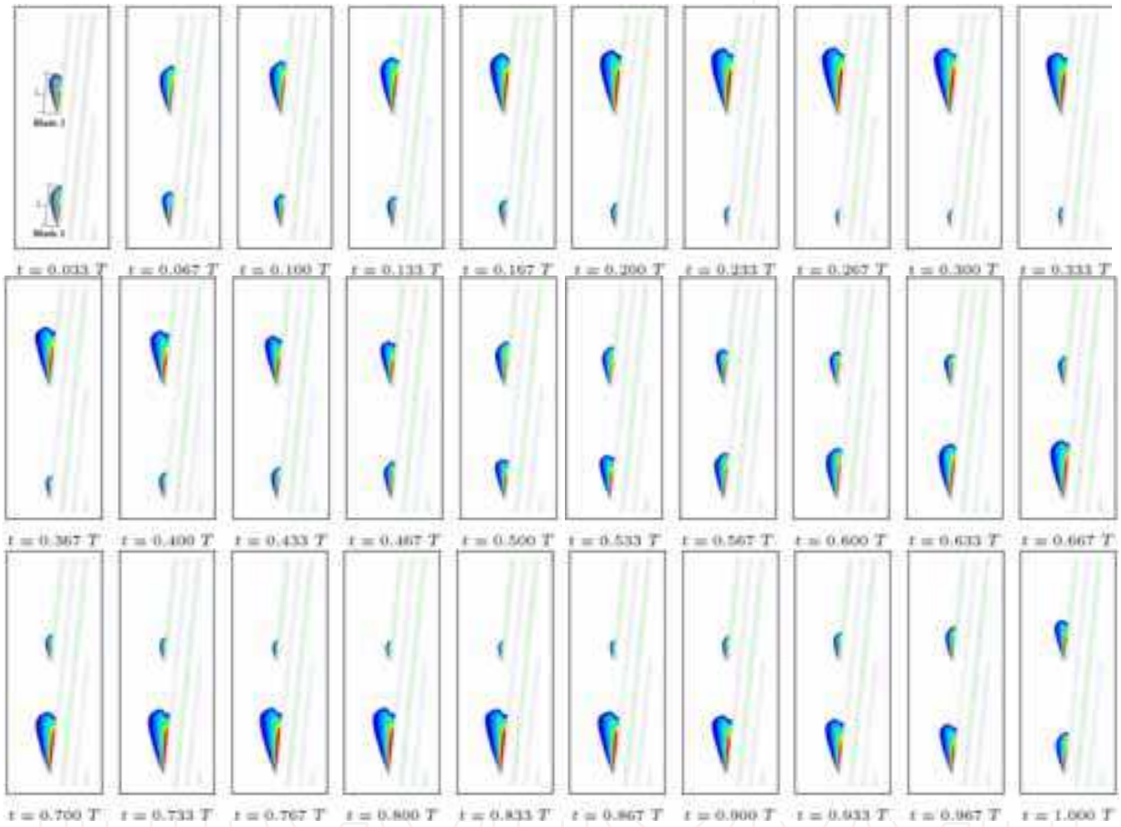

Fig. 9. Rotating blade cavitation on a two-blade inducer (σ=0.258 and Φ=0.039). Calculations using RNG κ-ε turbulence model

The vapour fluctuation has an unsteady cyclic behaviour, with a low frequency equal to $f_{cav}=0.07 \cdot f_{\omega}$ on one blade, see Fig. 10(a). The unsteady behaviour of the cavitation modifies the flow patterns which cause a pressure fluctuation upstream. The frequency analysis on the absolute frame gives a cavitating frequency of $f_{cav}=0.14 \cdot f_{\omega}$, because of the cavitation fluctuation on the two blades.

Fig. 10 shows the pressure coefficients measured on the two blades for the aircraft inducer and on the three blades for the industrial inducer. These ones were measured by virtual probes on the suction side of the blades inducers. These pressure fluctuations have been caused by the variation of the cavitation size attached to each blade. Rotating blade

cavitation was observed for two flow rate coefficients in the three-blade inducer. In these cases it was observed, at a certain time, two cavitations with the same size and another cavitation with a smaller size. This smaller cavitation moved in the same translational direction than the blade cascade, i.e. in the same rotational direction of the inducer; see Fig. 10(b). These cavitating fluctuations are cyclic with specific frequency. Table 3 resumes the frequencies of the rotating blade cavitation captured numerically for different flow rates and on different configurations.

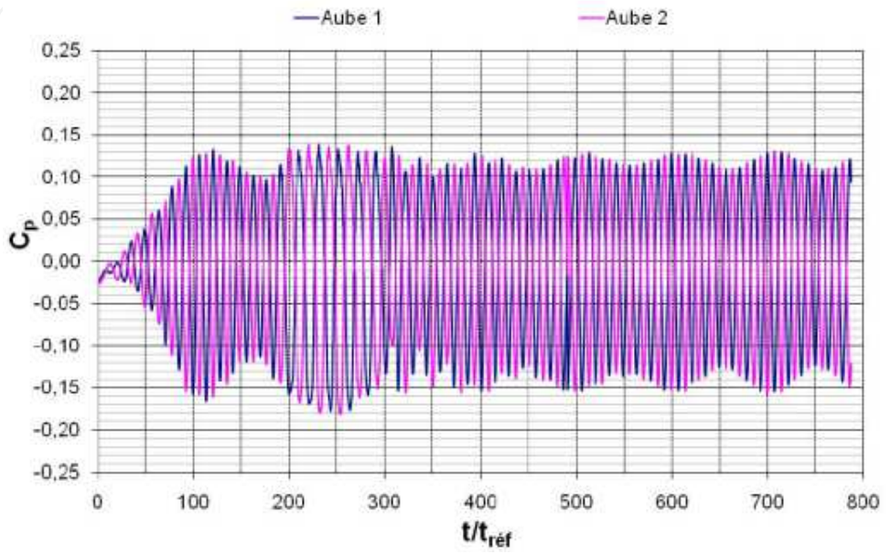

(a) Two-blade cascade

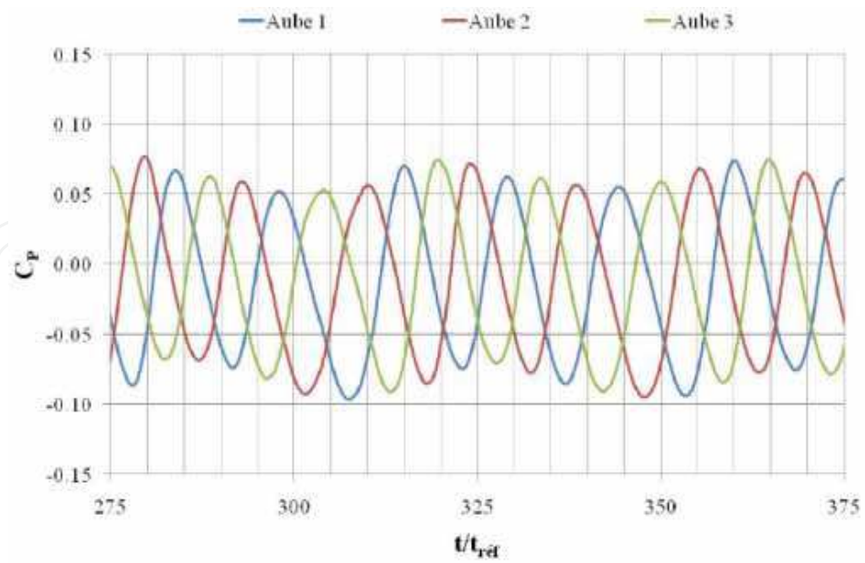

(b) Three blade cascade

Fig. 10. Pressure fluctuation on suction side of the blades caused by the variation of the length cavitation

3.2.2.3 Coupling of the intrinsic instabilities and the system instabilities

Numerical simulations were complemented using the RNG κ–ε modified turbulence model for $\sigma=0.258$ and $\Phi=0.039$. This modification allows the interaction between the system unsteadiness and the self–oscillation of the vapour region.

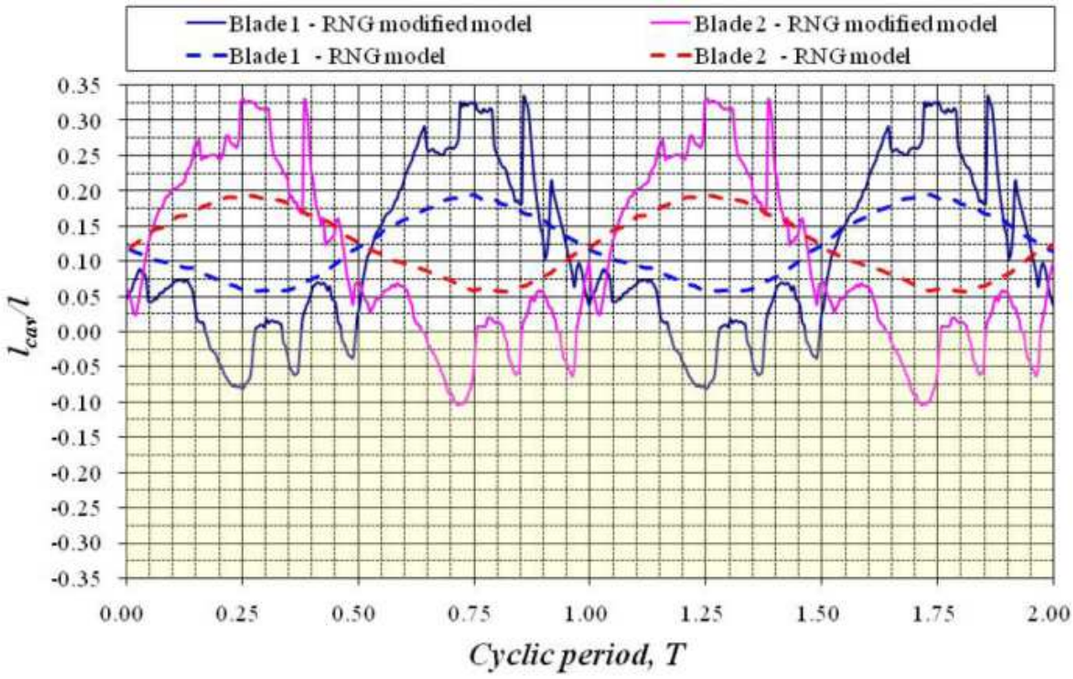

Fig. 11. Temporal evolution of the cavitation length. Calculations using RNG κ-ε and RNG κ-ε modified models

Fig. 12 presents the contours of vapour fraction at different times on a blades cascade. The cavitation shows a quasi–cyclical unsteady behaviour with a cavitation detachment frequency equal to $f_{cav}=0.06 \cdot f_{\omega}$ on relative frame and $f_{cav}=0.12 \cdot f_{\omega}$ on absolute frame.
The cavity has a similar cyclical unsteady behaviour than in the analysis using RNG κ–ε model, but now, the results show the vapour detachment ($t=0.833 \cdot T$ to $t=0.867 \cdot T_{cav}$, see Fig. 12, blade **1**), followed by its convection downstream ($t=0.900 \cdot T_{cav}$ to $t=0.933 \cdot T_{cav}$, see Fig. 12, blade **1**) and then, the cavitation passing from blade **1** to blade **2** at blades cascade throat ($t=0.967 \cdot T_{cav}$ to $t=1.0 \cdot T_{cav}$, see Fig. 12, blade **1** and blade **2**).
The curves of Fig. 11 show the temporal evolution of the cavitation length ($a \geq 10\%$) measured on each blade (e.g., $t=0.033 \cdot T_{cav}$ on Fig. 9), for both results calculations using RNG κ-ε and RNG κ-ε modified models. A negative cavitation length, for calculations using RNG κ-ε modified model, means that vapour region is attached to the pressure side of the neighbour blade. This phenomenon appears when the cavitation length of neighbour blade is large enough which produces the blockage of the channel flow. Thus, the fluid flow passes only through the other channel. All curves have a similar behaviour but the cavitation length is larger with the RNG κ–ε modified model than the RNG κ–ε model. The local length fluctuations observed on modified turbulence model are caused by the self–oscillation of the vapour region.

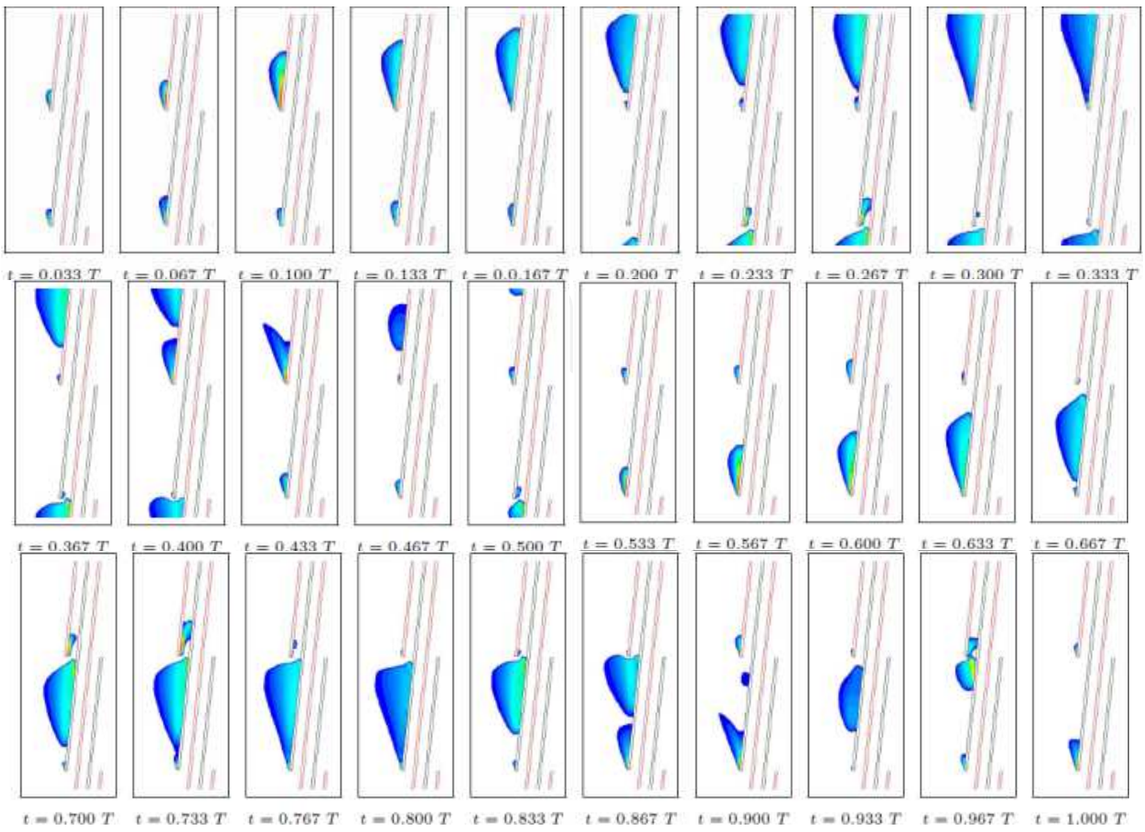

Fig. 12. Rotating blade cavitation on a two-blade inducer (σ=*0.258* and Φ=*0.039*). Calculations using RNG κ-ε modified turbulence model

3.3 Experimental study and numerical analysis of cavitating flows in three inducers

3.3.1 Experimental tests

Fig. 13. Bank of experimental tests from DynFluid laboratory (Arts et Métiers ParisTech), loop of the industrial inducers

The hydrodynamic bank used for the experimental tests consists of three independent closed loops. The first loop is adapted for test on the industrial inducers, see Fig. 13. The second loop is used for experimental tests of centrifugal pumps alone or coupled to an inducer. The third loop is adapted for aircraft-type inducers.

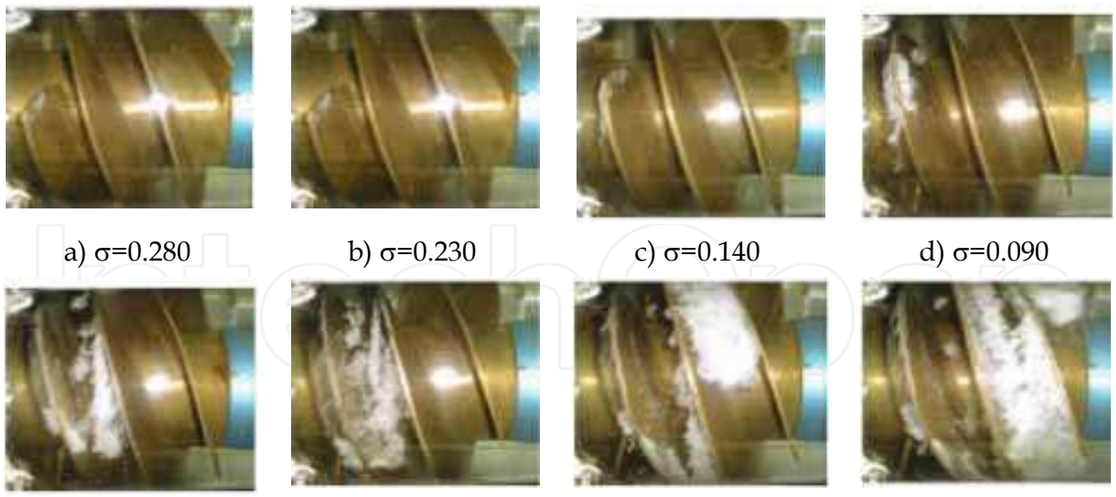

a) σ=0.280 b) σ=0.230 c) σ=0.140 d) σ=0.090

e) σ=0.060 f) σ=0.055 g) σ=0.050 h) σ=0.045

Fig. 14. Diverse cavitation forms obtained experimentally on a three-blade inducer with $\beta=16°$ ($\Phi=0.164$)

The industrial inducers loop consists mainly of the follow elements:

- Two tanks with a capacity of $4\ m^3$, connected by pipes of diameter of $350\ mm$.
- A vacuum pump adjusts the pressure at the free surface tank.
- A $22\ kW$ motor controls the rotational velocity. It is measured using a tachometer.
- A motorized valve is used to vary the fluid flow of the inducer.
- The inducer has a transparent casing allowing the observation of vapour structures (transparent cover).
- A temperature sensor. The average temperature during the tests was about $20\ °C$.

To capture the experimental structures of vapour through the transparent cover, it was used a digital camera under strobe lighting.

Fig. 14 shows the vapour formation at leading edge of a three blade inducer. The regions of vapour were mainly manifested in the form of three identical regions attached to each blade ($\sigma=0.280$). As the inlet pressure decreases, the cavitating structures suffer a growth phase, principally at tip leading edge of the blade (from $\sigma=0.230$ to $\sigma=0.090$), which move to down to the hub until they block the flow channel ($\sigma=0.060$ and $\sigma=0.055$). When the passage inter-blade is blocked by the vapour, the performance drop of the inducer occurs suddenly ($\sigma=0.050$ and $\sigma=0.045$). The gradual vapour apparition generates noise and vibrations. In this figure, each image corresponds to a value of σ for a flow rate constant.

The pictures obtained during the cavitation tests are typical cavitation forms and, in general, they are consistent with those reported by (Offtinger et al., 1996), see Fig. 14. Representative pictures were obtained from different experimental tests on the three studied inducers at partial flow rate, nominal flow rate and over-flow rate. As an example, some pictures obtained on a three-blade industrial inducer with blade tip angle of 16° are commented:

- The inception of the cavitation at leading edge of the tip blade, see Fig. 14(a-b).
- The formation of a tip tourbillon which captures the vapour, see Fig. 14(c).
- The cavitation grows in forms of vapour pockets which remain attached to the tip blade, see Fig. 14(d).

- The formation of a recirculation zone (backflow) which captures the vapour bubbles and becomes, with the low pressure, in the siege of a vapour region located on the leading edge of the tip blade. This cavitation tends to move in the opposite direction of the main flow, see Fig. 14(e-f).
- Blockage of the flow channel by the vapour which causes the performance drop of the inducer, see Fig. 14(g-h).

The formation of various type of cavitation is caused by the kinematics of the flow in the inducer. The numerical and experimental analyses suggest that the high velocity regions (favourable zone to cavitation inception) are localized to the inlet at partial flow rates, and toward the outlet at high flow rates.

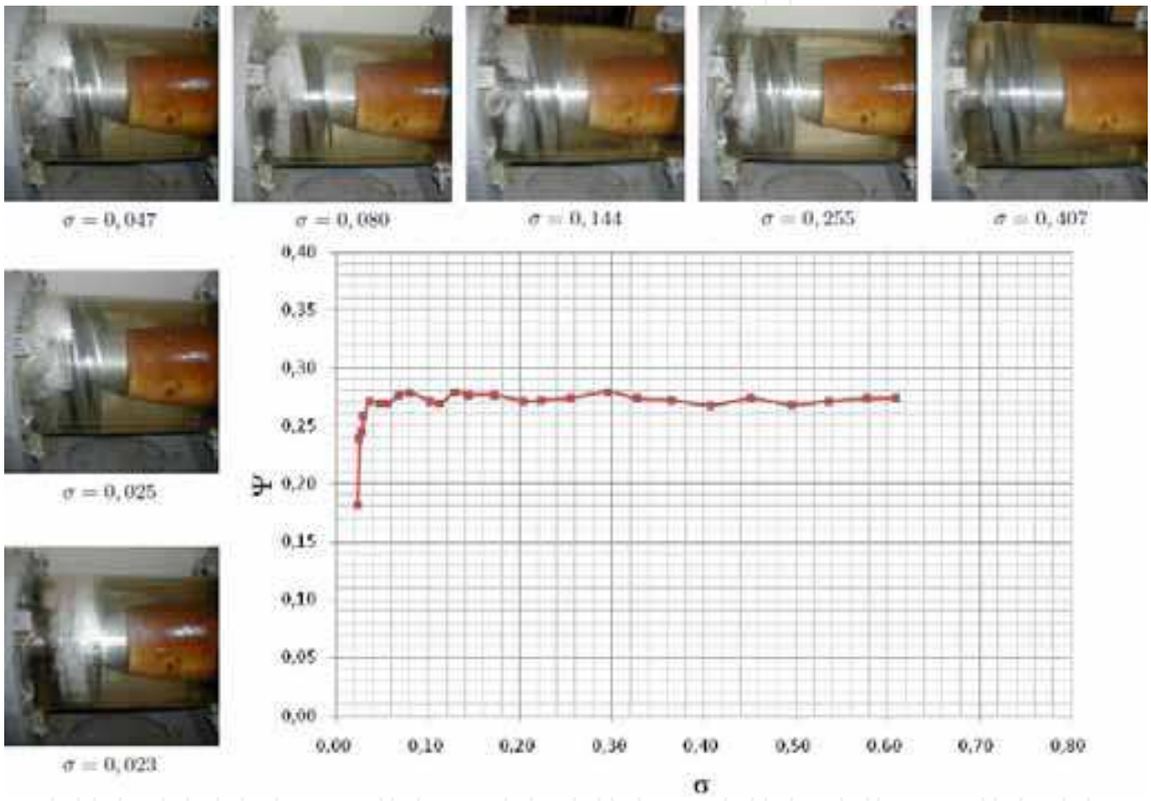

Fig. 15. Vapour behaviour for various cavitation conditions and its corresponding performance drop curve obtained experimentally on a three-blade inducer with β=8° (Φ=0.057)

3.3.2 Numerical analysis

3.3.2.1 Domain de control and grid generation

The numerical simulations, in steady and unsteady regime, were carried out on a two-blade aircraft inducer with a blade tip angle of 4°. In order of accelerate the calculation time, for the steady numerical simulations, only one third of the inducer was modelled. By contrast, this simplification could not be considered for the unsteady calculations because the instabilities of the cavitating flow are influencing by the neighbour blades (system instabilities).

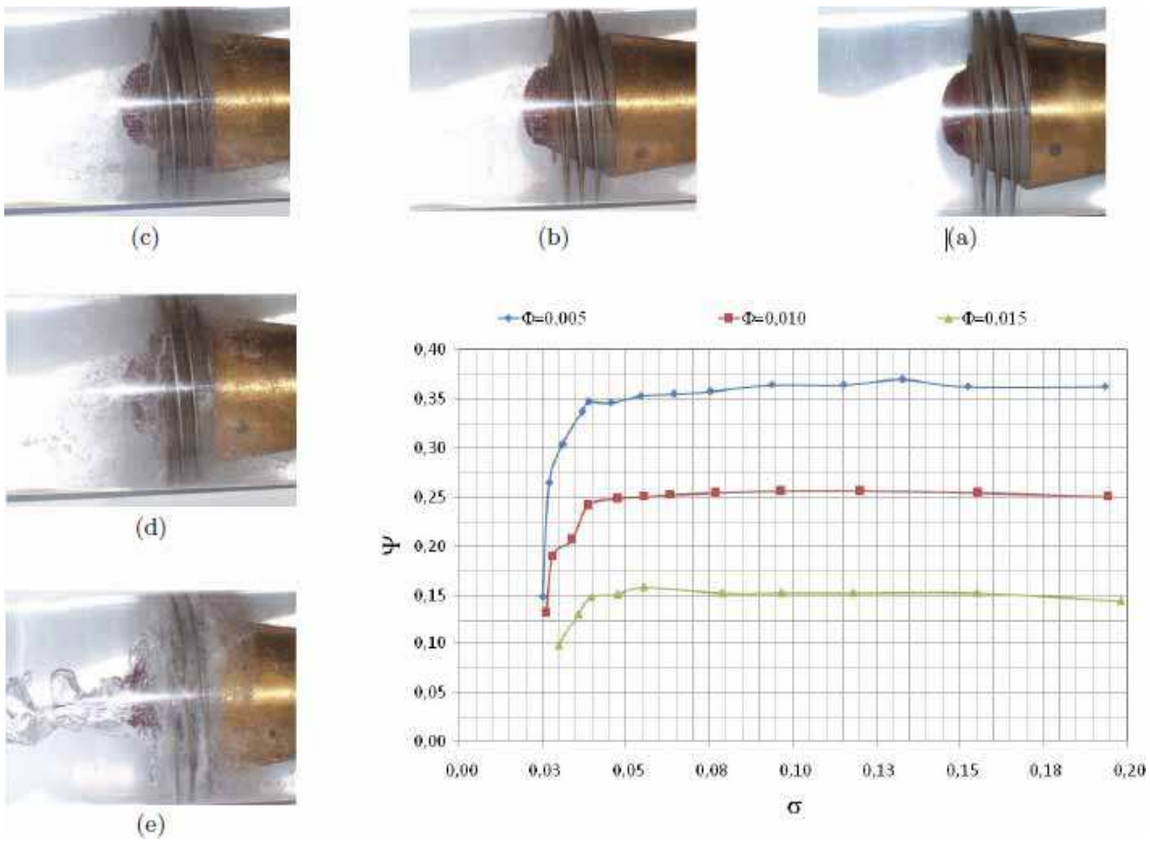

Fig. 16. Vapour behaviour for different cavitation conditions and its corresponding performance drop curve obtained experimentally on a two-blade inducer (Φ=*0.005*)

Many three-dimensional hybrid grids were generated using the pre-processor *Gambit*. The computational domain was divided into four sub–blocks in order to facilitate the grid generation. The sub–blocks are located as follow, see Fig. 17:

- **Inlet region**, lengthened *2.6* D_t upstream of the blade leading edge;
- **Blade to blade region**, which includes the flow channels formed by the blades;
- **Outlet region**, extended *2.4* D_t downstream of trailing edge; and
- **Tip clearance region**, modelled by a ring of thickness δ_t and an axial length l_{rotor}.

The grid process starts by meshing, with 2D triangular type cells, the blades surfaces. Then, the blade to blade region was meshed with 3D tetrahedral type cells. The tip clearance and blade to blade regions were meshed using smaller size cells than inlet and outlet regions, which were meshed with prism type cells, see Fig. 18. One conformal grid interfaces were used at the boundary of the regions "blade to blade – tip clearance". Two non–conformal grid interfaces were used at the boundary of the regions "upstream – blade to blade" and "blade to blade – downstream", see Fig. 17. Fig. 18 shows the surface grid on the rotor and the meridional view which is noticed the tip clearance grid.

For the grid independence study, four computational grids were tested. All these were generated with the same meshing strategy, but they are different in the cells number. The grid sizes are: (a) 480,185; (b) 1, 050,154; (c) 1,528,668; and (d) 1,996,418. The numerical results in steady state were compared to the experimental data. The first two grids show

variations on the numerical results because of a poor grid used. The last two grids give approximately the same than the experimental data but the grid (d) makes a lot of computational time to find the solution. For this reason, the grid (c) was selected for carried out the numerical results.

Finally, a grid dependence study to model the radial tip clearance was made. Fist, different grid types were tested, see Fig. 19. The first two grids were generated automatically on only one region which merges the blade to blade region and the tip clearance region. In this type of grids is very difficult to control the mesh near to wall, particularly the space formed between the tip blade and the carter, so the grid (d) on Fig. 19 was selected because it uses two blocks to defines the blade to blade and tip clearance regions and a conformal grid interfaces between both regions. Second, the grid density was varied from 5, 15, 25 and 30 equidistant cells in radial direction.

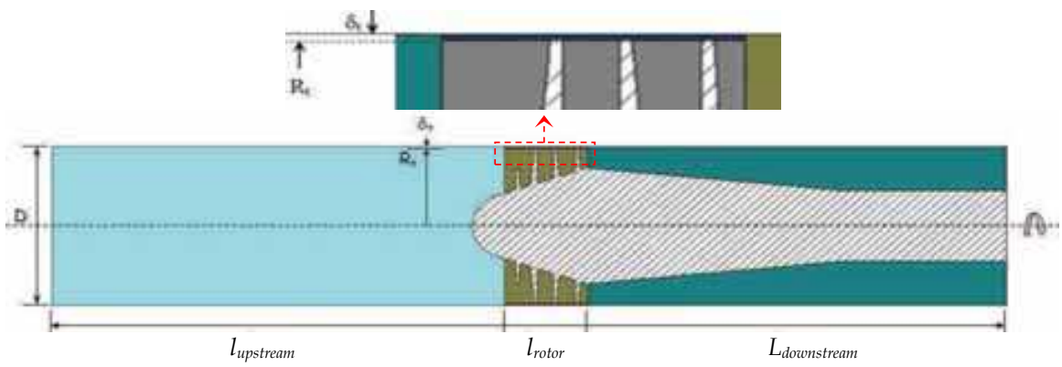

Fig. 17. Different blocks which form whole of the computational domain

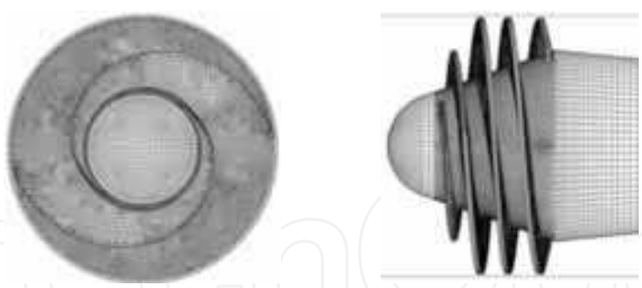

(a) Front view (b) Lateral view

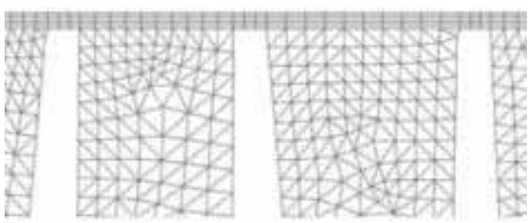

(c) Meridional view

Fig. 18. Computational grid used for the numerical simulations

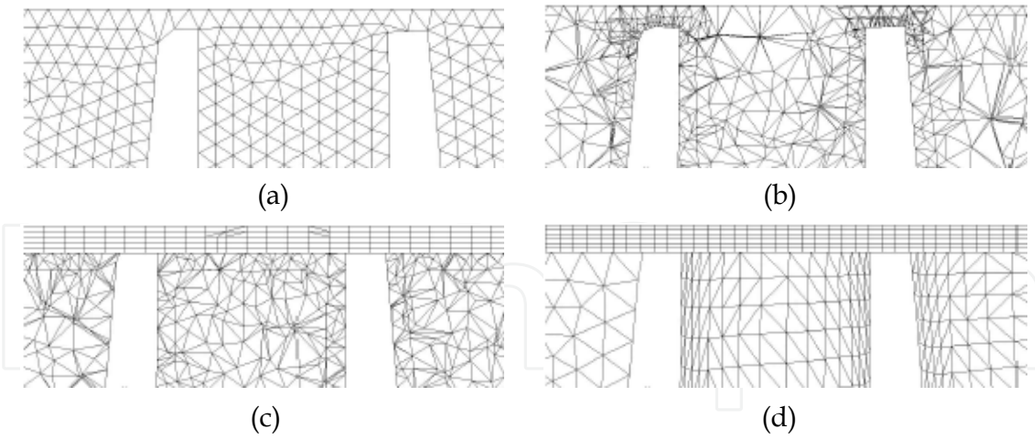

Fig. 19. Tip clearance grids tested

3.3.2.2 Numerical results in steady state

The numerical simulations in steady state were carried out for the three inducers presented on the Fig. 1. The cavitating calculations were realized on one flow channel of the inducers using periodical conditions for different flow rates (partial flow rates, nominal flow rates and over-flows), and for various cavitation conditions (σ). By way of example, the Fig. 20 shows the diverse cavitation forms which rise as the cavitation number decreases. It is

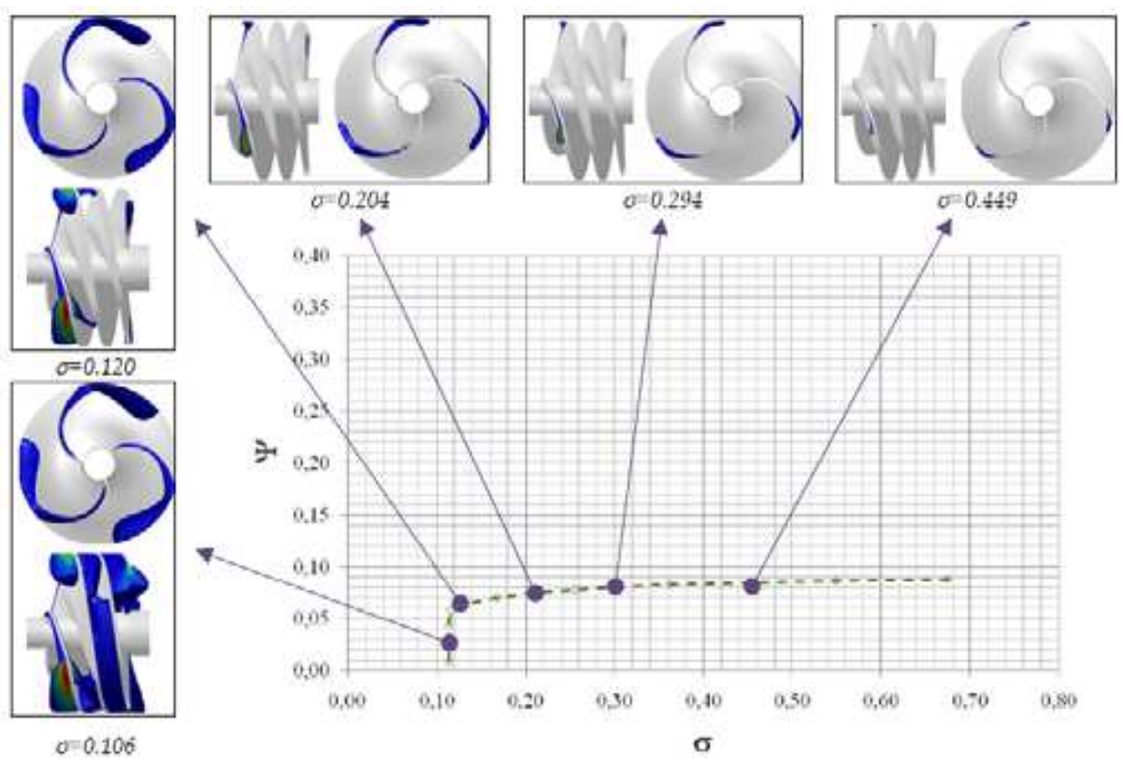

Fig. 20. Vapour behaviour for different cavitation conditions and its corresponding performance drop curve obtained numerically on a three-blade inducer with β=8° (a≥15 and Φ=0.112)

possible to observe that, as numerical as experimentally, at the inception of cavitation, the vapour appears in form of triangle at leading edge, and it is extended at tip blade as far as to cause the flow channel blockage.

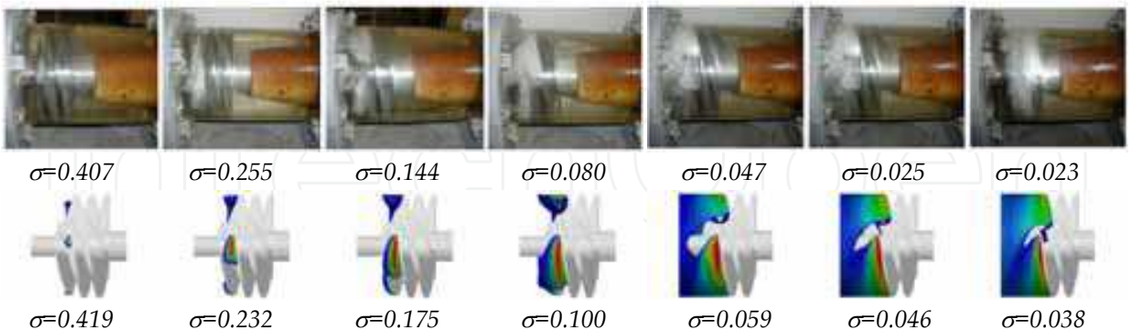

Fig. 21. Qualitative comparison of cavitation between experimental tests and numerical results on a three-blade inducer with β=8° (a≥15% and Φ=0.079)

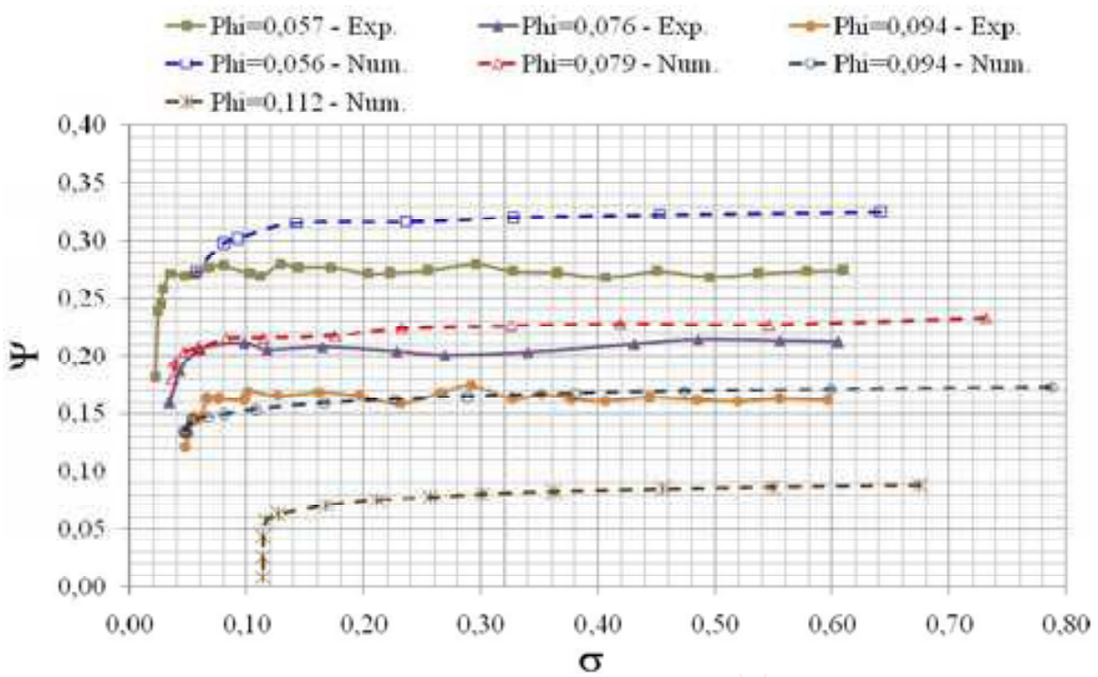

Fig. 22. Quantitative comparison of cavitation between experimental tests and numerical results on a three-blade inducer with β=8°

The numerical results obtained in steady state were compared as much qualitatively as qualitatively to the experimental tests. Fig. 21 shows a qualitative comparison of cavitation behaviour on a three-blade inducer with blade tip angle of 8°.
The cavitating analyse find a fluid flow more instable, during the numerical simulations and experimental tests, in the partial flow rates than in the over-flows. In the Fig. 20 is possible to note that, when the performance drop arrives, the flow channel is filled by the vapour for an over-flow (Φ=0.112) unlike a partial flow rate (Φ=0.079) in the Fig. 21. On the other hand,

the main difference found on the curves of the Fig. 22 was to the partial flow rate where the performance drop was predicted faster by the calculation than the experimental tests.
Fig. 22 shows a comparison of the performance drop curves obtained numerical and experimentally where is possible to observer a good coherence of the results. The differences found between numerical results and experimental data are, amongst others, attributing to that:

- The numerical simulations were carried out on only one flow channel using cyclical conditions; consequently, the fluid flow is perfectly identical on the three flow channels. This configuration does not consider the interaction between the flow channels.
- The numerical simulations suppose that the inducer has parfait geometry, without manufacturing defects and composed of identical blades.
- The experimental back elements located upstream and downstream were negligee.
- The numerical model does not consider the radial tip clearance.

3.3.2.3 Numerical results in unsteady state

The numerical simulations in unsteady state were carried out from the results obtained in steady state for a two-blade inducer with tip blade angle of 4° described in the Fig. 1. The calculations were realized to partial flow rates, where more instability problems were detected in the previous experimental and numerical cavitating analyse.

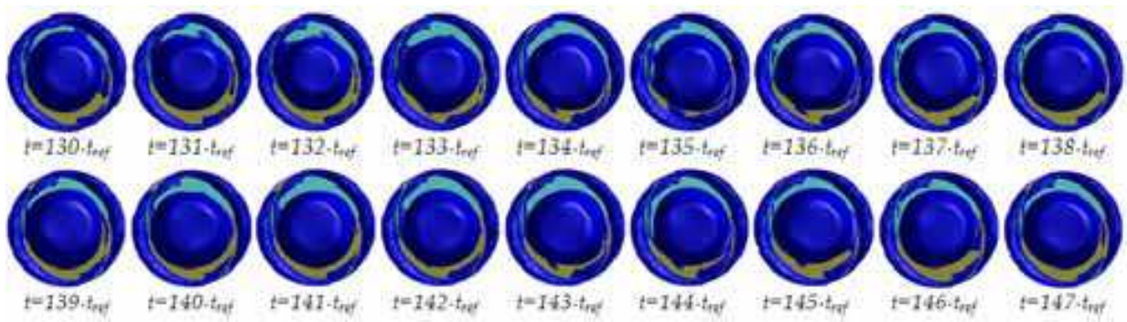

Fig. 23. Temporal evolution of the vapour (α=*20%*) in the two-blade inducer (Φ=*0.0050* and σ=*0.064*), front view

The reference time was defined as the inducer rotating period, $t_{ref}=T_{\omega}$=*7.5E-3 s*. The time step, used for all numerical simulations, was calculated, after a temporal independence study, for an angular moving of 3.6°; then, the time step was defined as $\Delta t=t_{ref}/100$=*7.5E-5 s*.
It is important to underline that the unsteady calculations needed about 80 iterations by time step, resulting in 8,000 iterations by one inducer turn. The numerical stability was noted after 50 inducer turns, i.e. it was necessary at least 400,000 iterations to start to observe the instabilities caused by the cavitating flow in the inducer… if these ones exist at these flow conditions (Φ and σ). In considering that, the calculations were developed on an 8 processors cluster, with a calculation time of about 10 *s/iteration*, the unsteady calculations can take more than two months (time of machine) for a constant flow rate and a specific cavitation number. The very long calculating time, combined with the high capacity of storage, necessary for the post-processing stage, make very difficult to realize successfully the numerical calculations in unsteady state. Moreover, the analysis of the results requires a hard work to find the instabilities.

Knowingly the hard work needed to detect the instabilities by 3D numerical simulations; the results obtained to Φ=0.0050 and σ=0.064 are presented, in different views, on the Fig. 23, Fig. 24 and Fig. 25. The pictures were obtained when all flow parameters were stabilized (after $t=130\cdot t_{ref}$). This figure shows the temporal evolution of the vapour ($\alpha \geq 20\%$) in the two-blade aircraft inducer with blade tip angle of 4°. Eighteen instants can be observed between $t=130\cdot t_{ref}$ and $t=147\cdot t_{ref}$, each picture corresponds to one inducer turn (t_{ref}).

These three figures show the cavitation has a crown form located at the periphery of the inducer. Another vapour region, with shape of the torch is located upstream, see Fig. 24 and Fig. 25. In certain instants, both cavitations, this one located at the periphery and the other one in form of torch, are connected by a narrow vapour region formed along the leading edge, from the tip blade to the inducer hub.

The cavitation develops gradually on the leading edge of the blade **2** (green blade), and it becomes bigger than on the blade **1** (blue blade) at $t=135\cdot t_{ref}$. Later, the cavitation decreases gradually on the blade **2** until $t=140\cdot t_{ref}$. In contrast, at this instant, the cavitation on the leading edge of the blade **1** is the biggest. Finally, the size cavitation increases again on the blade **2** and it decreases on the blade **1** at $t=144\cdot t_{ref.}$

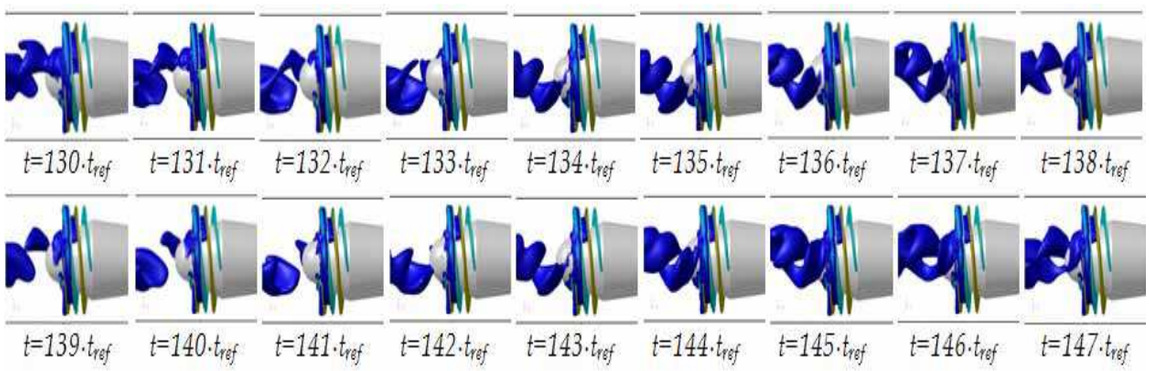

Fig. 24. Temporal evolution of the vapour ($\alpha=20\%$) in the two-blade inducer ($\Phi=0.0050$ and $\sigma=0.064$), lateral view

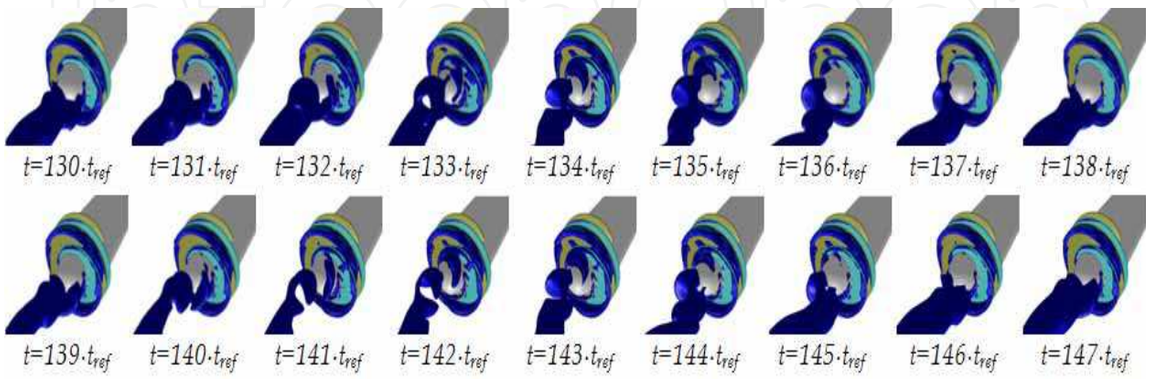

Fig. 25. Temporal evolution of the vapour ($\alpha=20\%$) in the two-blade inducer ($\Phi=0.0050$ and $\sigma=0.064$), isometric view

In conclusion, this fluctuation of cavitation size is almost cyclic, as observed previously in the analysis of the 2D unsteady cavitating flow. As can be seen in the figure, the cavitation length is maximal at the instants $t=135 \cdot t_{ref}$ and $t=144 \cdot t_{ref}$ on the blade **2** and at the instants $t=131 \cdot t_{ref}$ and $t=140 \cdot t_{ref}$, and $t=149 \cdot t_{ref}$ on the blade **1**.
The period of the cavitation fluctuation is $T_{cav}=0.0675\ s$ and its frequency $f_{cav}=14.8\ Hz$. The fluctuations can be driven by the cavitation torch formed upstream of the inducer. The torch turns in the same direction, but with a lower rotational velocity of the inducer. So, the torch turns 1 time while the inducer turns 9 times, as can be observed on the Fig. 23. The unsteady cavitating calculations were performed, in the first place, for $\sigma=0.064$. Then, from this unsteady results, the calculations were realized for $\sigma=0.051$, and then, for $\sigma=0.043$. This last calculation corresponds about *10%* of the inducer performance drop curve. In this case, one cavitation fluctuation occurs each 22 inducer turns. Thus, the cavitation fluctuation period is $T_{cav}=0.0600\ s$ and its frequency $f_{cav}=16.7\ Hz$, for $\sigma=0.043$.

4. Conclusion

Steady and unsteady numerical simulations were carried out in many configurations: first, in a venturi duct, next in two blades cascades with different characteristics, and then, in three axial inducers.
In order to understand the cavitation behaviour in the inducers and to validate the steady results obtained numerically, many experimental tests were developed, in steady state, for the three studied inducers.
In general, a good agreement between experimental and predicted results was found for a range of flow rates and cavitation behaviour, i.e., overall performances, cavities sizes and cavities location, etc. This study shows that the optimal inducer design depends mainly on three criterions to choose the best design for the three studied inducers: The critical cavitation coefficients corresponding to 5% and 15% of head drop, the head and efficiency produced in cavitating and non-cavitating conditions, and the vibrations generated by the inducers operations.
The numerical results, in a simple geometry, suggest a strong interaction of the turbulence and the unsteady cavitation.
Cavitating flow in the blades cascades, for various values of σ and flow rates, predicted three types of cavitation behaviour on the blades cascade:

a. Stable behaviour with symmetrical cavitation length,
b. Stable behaviour with non–symmetrical cavitation length, observed only for a two-blade inducer, according experimental observations (Tsujimoto, 2001)
c. Cyclical unstable behaviour with non–symmetrical cavitation length.

Symmetrical cavitations on all the blades were observed for high values of σ and high flow rates. Alternate blade cavitation was observed numerically for partial flow rates, when the *l/h* ratio was higher than about *65%*. This phenomenon was observed only on the two-blade inducer. Finally, the rotating cavitation was observed for lower flow rates, on both studied blades cascades. The calculations were carried out using RNG κ–ε model and RNG κ–ε modified model which provide different results.
Unsteady numerical results showed three different mechanisms of cavitation instabilities:

- Self–oscillation of the cavitation due to the interaction between the recirculation flow and the cavity surface (intrinsic instability).

- Rotating cavitation due to the interaction of one cavitation attached to a blade with the leading edge of the neighbouring blade (system instability).
- Coupling of the rotating cavitation and the self–oscillating of the cavitation (combination of intrinsic and system instabilities).

Finally, the unsteady cavitating calculations realized in three-dimensions for a two-blade inducer demonstrate the complexity to obtain and analyze the flow instabilities caused by the cavitation in these machines. The obtained results show that rotating cavitation appears for a partial flow rate, but it is less obvious in the inducer than in the blades cascade. It was noted that the shape and behaviour of cavitation is greatly disturbed by the tip radial clearance, which also modifies the torch which is formed upstream.

5. References

Bakir, F., Kouidri, S., Noguera, R. & Rey, R. (2003). *Experimental analysis of an axial inducer influence of the shape of the blade leading edge on the performances in cavitating regime*, Journal of Fluids Engineering, Transactions of the ASME, Vol. 125(2), pp. 293-301.

Campos-Amezcua, R., Khelladi, S., Bakir, F., Mazur-Czerwiec, Z., Sarraf, C., & Rey, R. (2010) *Numerical analysis of unsteady cavitating flow in an axial inducer*, Proceedings of the Institution of Mechanical Engineers, Part A: Journal of Power and Energy, Vol. 224(2), pp. 223-238.

Campos-Amezcua, R. (2009). *Analyse des écoulements cavitants stationnaires et instationnaires dans les turbomachines*, PhD thesis. Arts et Métiers ParisTech - Laboratoire d'Energétique et Mécanique des Fluides Interne, Paris, France.

Mejri, I., Bakir, F., Rey, R. & Belamri, T. (2006). *Comparison of computational results obtained from a homogeneous cavitation model with experimental investigations of three inducers*, Journal of Fluids Engineering, Transactions of the ASME, Vol. 128(6), pp. 1308-1323.

Kim, S.E., Mathur, S.R., Murthy, J.Y. & Chouhury, D. (1998). *A Reynolds–Average Navier–Stokes solver using unstructured mesh based finite–volume scheme,* 36th Aerospace Sciences Meeting and Exhibit, Reno, NV.

Offtinger, C. Henry, C. & Morel, R. (1996). *Instabilité de fonctionnement en débit partiel d'un inducteur fretté and comparaison avec le cas non fretté,* 3ème journée on cavitation, SHF. pp. 31–38. Grenoble, France.

Reboud, J., Stutz, B. & Coutier-Delgosha, O. (1998). *Two-phase flow structure of cavitation: Experiment and modelling of unsteady effects,* 3rd Int. Symp. Cavitation. April 7-10, Grenoble, France.

Singhal, A.K., Athavale, M.M., Li, H.Y. & Jiang, Y. (2002). *Mathematical basis and validation of the full cavitation model*, J. Fluids Eng. Vol. 124(3), pp. 617–624.

Stutz, B. & Reboud, J. L. (2000). *Measurements within unsteady cavitation,* Exp. in Fluids. Vol. 29, pp. 245–552.

Tsujimoto, Y., Horiguchi, H. & Qiao, X. (2005). *Backflow from inducer and its dynamics*, 5th Pumping Machinery Symp., June 19–23, Houston, Texas.

Tsujimoto, Y., Kamijo, K., & Brennen, C. (2001). *Unified treatment of flow instabilities of turbomachines,* J. propulsion and power. Vol. 17(3), pp. 636-643.

Yakhot, V. & Orszag, A.S. (1986). *Renormalization group analysis of turbulence–Basic theory,* J. Scientific Computing. Vol. 1(1), pp. 3–51.
Wilcox, D.C. (1998). *Turbulence Modeling for CFD*, DCW industries. La Canada, California.

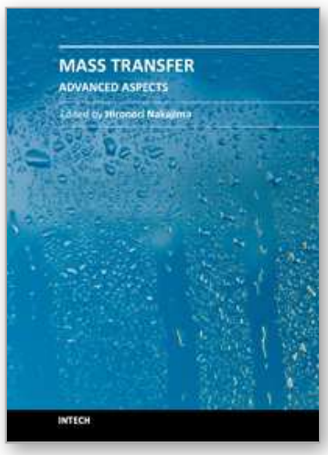

Mass Transfer - Advanced Aspects

Edited by Dr. Hironori Nakajima

ISBN 978-953-307-636-2
Hard cover, 824 pages
Publisher InTech
Published online 07, July, 2011
Published in print edition July, 2011

Our knowledge of mass transfer processes has been extended and applied to various fields of science and engineering including industrial and manufacturing processes in recent years. Since mass transfer is a primordial phenomenon, it plays a key role in the scientific researches and fields of mechanical, energy, environmental, materials, bio, and chemical engineering. In this book, energetic authors provide present advances in scientific findings and technologies, and develop new theoretical models concerning mass transfer. This book brings valuable references for researchers and engineers working in the variety of mass transfer sciences and related fields. Since the constitutive topics cover the advances in broad research areas, the topics will be mutually stimulus and informative to the researchers and engineers in different areas.

How to reference

In order to correctly reference this scholarly work, feel free to copy and paste the following:

Rafael Campos-Amezcua, Sofiane Khelladi, Zdzislaw Mazur-Czerwiec, Farid Bakir, Alfonso Campos-Amezcua and Robert Rey (2011). Numerical and Experimental Study of Mass Transfer Through Cavitation in Turbomachinery, Mass Transfer - Advanced Aspects, Dr. Hironori Nakajima (Ed.), ISBN: 978-953-307-636-2, InTech, Available from: http://www.intechopen.com/books/mass-transfer-advanced-aspects/numerical-and-experimental-study-of-mass-transfer-through-cavitation-in-turbomachinery

INTECH
open science | open minds

InTech Europe
University Campus STeP Ri
Slavka Krautzeka 83/A
51000 Rijeka, Croatia
Phone: +385 (51) 770 447
Fax: +385 (51) 686 166
www.intechopen.com

InTech China
Unit 405, Office Block, Hotel Equatorial Shanghai
No.65, Yan An Road (West), Shanghai, 200040, China
中国上海市延安西路65号上海国际贵都大饭店办公楼405单元
Phone: +86-21-62489820
Fax: +86-21-62489821

IntechOpen